ELSEVIER

Computational Materials Science 5 (1996) 157–166

COMPUTATIONAL MATERIALS SCIENCE

A biomimetic example of brittle toughening: (I) steady state multiple cracking

Hannes Kessler [a], Roberto Ballarini [b], Robert L. Mullen [b], Liisa T. Kuhn [c], Arthur H. Heuer [a]

[a] *Department of Materials Science & Engineering, Case Western Reserve University, 10900 Euclid Avenue, Cleveland, OH 44106, USA*
[b] *Department of Civil Engineering, Case Western Reserve University, 10900 Euclid Avenue, Cleveland, OH 44106, USA*
[c] *Children's Hospital, Orthopedic Research, 300 Longwood Avenue, Boston, MA 02115-5737, USA*

Received 15 July 1995; accepted 31 August 1995

Abstract

Multiple cracking dissipates energy and thus enhances the toughness of materials and structures composed of relatively brittle constituents. In this paper a biomimetic example is studied, i.e. the fracture behavior of the conch shell (*Strombus Gigas*). We focus on multiple cracking which occurs in the macroscopic layer on the tensile side of 4-point bend specimens with the crossed-lamellar microstructure. The interaction between the cracks results in mutual shielding and thus a lower stress intensity factor at each crack tip. An approximate fracture mechanics model of this mechanism is presented.

1. Introduction

It is well known that multiple cracking dissipates energy and thus enhances the toughness of materials and structures composed of relatively brittle constituents [1]. In this contribution we present and analyze a biomimetic example. Inspired by earlier investigations [2], we studied the fracture behavior of the conch shell (*Strombus Gigas*, Fig. 1). The conch shell consists of 99.9% aragonitic $CaCO_3$, arranged in the so-called crossed-lamellar structure (Fig. 2, Ref. [3]). Lamellae of three size scales are assembled into three or more macroscopic layers of 1 to 4 mm thickness. The orientation of the 1st-order lamellae, which represent the largest size scale with a thickness of ~ 40 μm, changes by 85° to 90° from one layer to the next. The lamellae and the macroscopic layers are separated by weak and thin organic (proteinaceous) interfaces. Samples prepared from the shell were tested in 4-point bending, load–displacement curves being recorded, and strength and work of fracture were determined. Details of the experimental procedure and the fracture mode are given in Ref. [4]. In this paper, we focus on multiple cracking which occurs in the macroscopic layer on the tensile side of 4-point bend specimens of shells with the crossed-lamellar microstructure (Fig. 3). The interaction between the cracks results in mutual shielding and thus a lower stress intensity factor at each crack tip, compared to a singly cracked specimen. This in turn leads to a higher failure stress and strain. Below, we present an approxi-

SSDI 0927-0256(95)00067-4

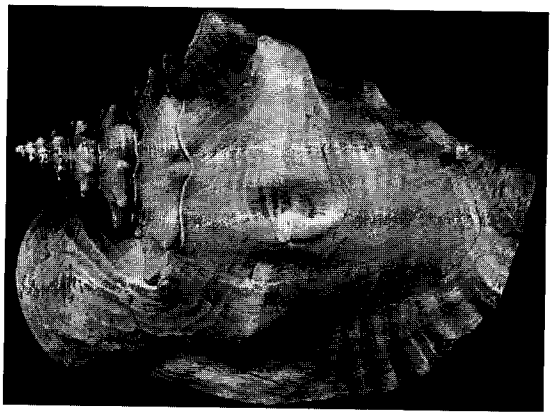

Fig. 1. Species of the conch shell (Strombus Gigas). The maximum size of the animal is 25–30 cm. Its shell is optimized to withstand attacks of crabs, which try to reach the living organism. Damage tolerance is of the almost importance.

mate fracture mechanics model of this mechanism, which allows us to identify the primary parameters influencing the toughening.

2. Model of multiple cracking and failure

2.1. Higher work of fracture by multiple cracking: the basic idea

To gain an understanding of the effects of multiple cracking, we replace the composite structure shown in Fig. 2 with the plane strain configuration shown in Fig. 4. The three anisotropic macroscopic layers, which are inhomogeneous on the size scale of the lamellae, are modeled by two homogeneous isotropic layers with identical elastic moduli E, but different fracture toughnesses, K_{c1} and K_{c2}. The specimen of length L is loaded in tension through prescribed displacements u_L. The cracks of length t_2 will propagate catastrophically through the stronger upper strong layer at a stress intensity given by

$$K_I = K_{c1} = \sqrt{\frac{2\gamma_1 E}{1-\nu^2}}, \tag{1}$$

where K_I, K_{c1}, γ_1, E and ν are the stress intensity factor at the tip of one of the multiple cracks, the plane strain fracture toughness and the crack surface energy of the strong layer, Young's modulus and Poisson's ratio, respectively. Dimensional analysis demands that the stress intensity factor K_I depends linearly on the applied nominal tensile stress σ times the square root of a characteristic length of the problem, i.e. the crack spacing a, the crack length t_2, or the uncracked ligament size t_1. The asymptotic dependencies of the stress intensity factor of specimens that are not deeply cracked are given by

$$K_I \sim \sigma \times \begin{cases} t_2^{1/2} & \text{if } a \gg t_2 \\ a^{1/2} & \text{if } a \le t_2 \end{cases}. \tag{2}$$

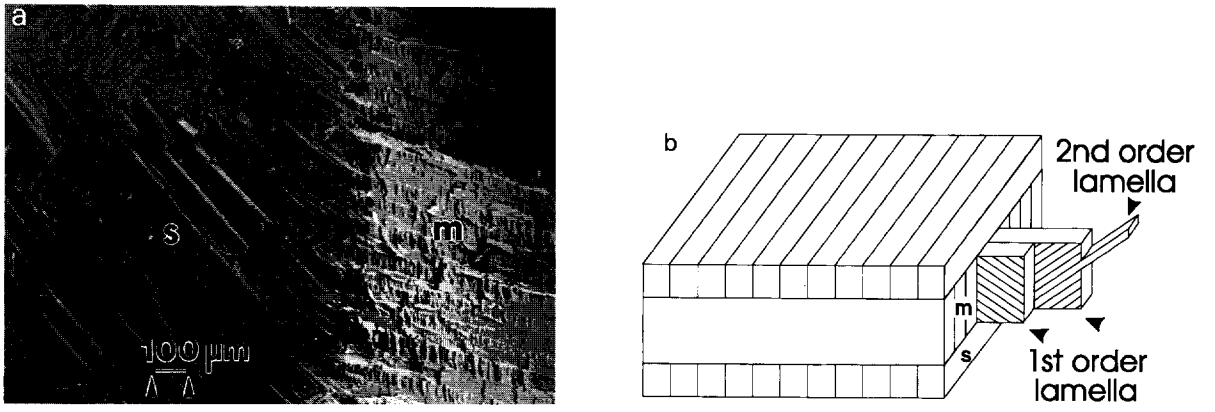

Fig. 2. Crossed-lamellar microstructure of the conch shell. (a) Fracture surface showing the 1st-order lamellar structure in two adjacent macroscopic layers. Fracture occurred along a 1st-order interface in the left hand layer 's'; thus the 1st-order lamellae remained undamaged. In the right hand layer 'm' the 1st-order lamellae were fractured due to their orientation being perpendicular to the direction of crack propagation. (b) Schematic drawing of the 1st- and 2nd-order lamellar structure in three macroscopic layers. The fracture surface, with surface layer 's' and middle layer 'm' from (a), is indicated (but rotated by 90°).

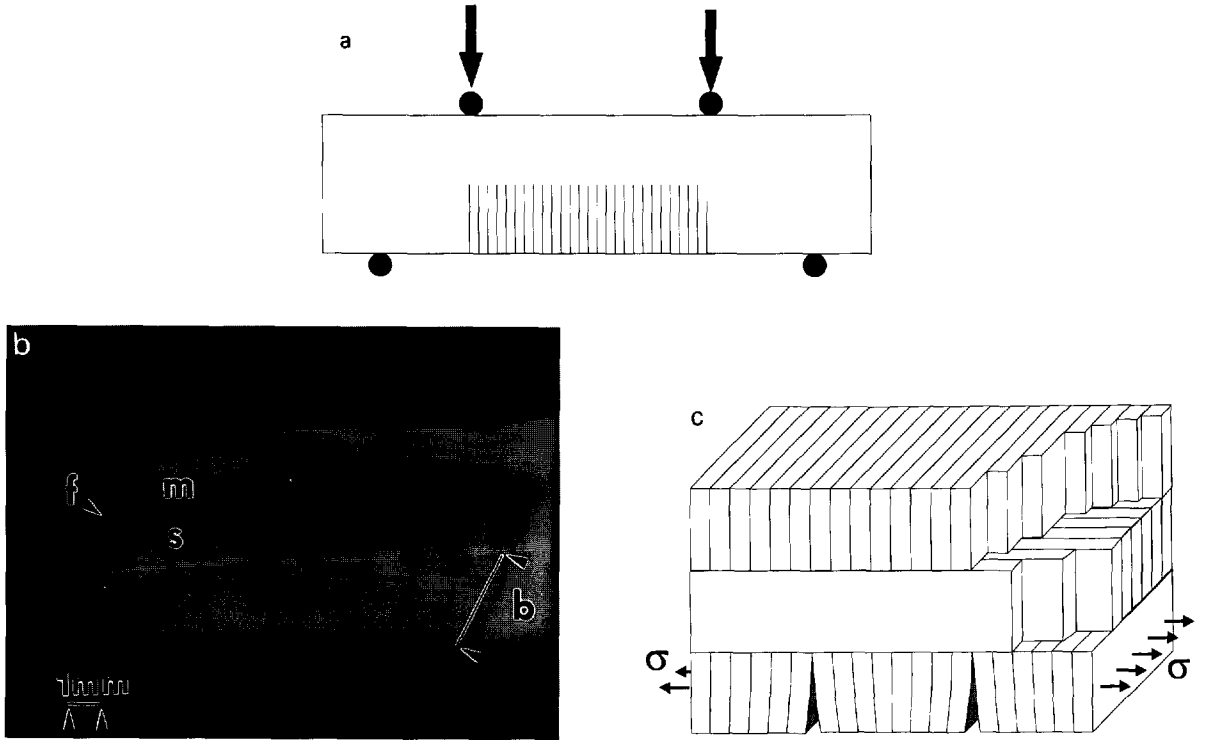

Fig. 3. Multiple cracking in the macroscopic layer on the tensile side in a 4-point bend test (sample orientation corresponds to the front view of Fig. 2b). The 1st-order interfaces in the tensile layer are oriented perpendicular to the tensile stress. Multiple cracks propagate easily along these weak interfaces in the surface layer and stop when they reach the middle layer. The surface layer and the middle layer are referenced in the following as 'weak' layer, and 'tough' or 'strong' layer, respectively. (a) Schematic drawing of observed multiple cracking in a 4-point-bend test. (b) Optical micrograph of multiple cracks in a remnant of a fractured 4-point bend specimen. Multiple cracks are made visible by a dye penetrant. The side of the fracture surface ('f', not visible) is indicated. The weak layer 's' and the strong layer 'm' are visible in the front view; the weak layer is also visible from the bottom of the sample. Multiple cracks in the weak layer span the sample width b. (c) Schematic drawing of two cracks at 1st-order interfaces and the orientation of 1st-order lamellae with respect to the tensile stress σ.

Therefore, if multiple cracking is favored by a low fracture toughness of the weak layer ($K_{c2} < K_{c1}$), which leads to small crack spacings a, a higher nominal stress σ has to be applied in order to reach the failure condition Eq. (1). Additionally, the higher compliance of the multiply cracked specimens leads to an increase in the nominal failure strain. The combined effects of higher failure stress and higher failure strain result in a higher work of fracture.

2.2. Multiple cracking criterion

Under a nominal strain ε, the total energy of the system, U_{total}, consists of the crack surface energy U_{surface} and the strain energy U_{strain}. Both energies are functions of the crack density, defined as $n = t/a$, where $t = t_1 + t_2$ denotes the specimen thickness. We adopt the criterion that

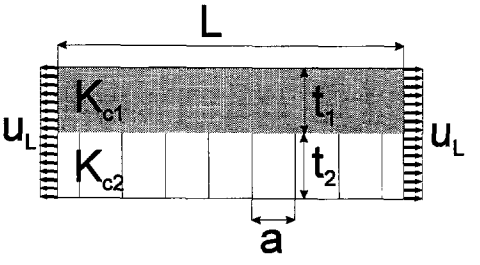

Fig. 4. Physical model of the multiple-crack toughening effect.

the crack density is governed by the following strain-controlled minimum energy condition:

$$U_{\text{total}}(n, \varepsilon) = U_{\text{surface}}(n) + U_{\text{strain}}(n, \varepsilon) = \min(n). \tag{3}$$

Thus the crack density can be calculated as a function of the applied nominal strain by setting the partial derivative of the total energy with respect to the crack density to zero:

$$\left(\frac{\partial U_{\text{total}}}{\partial n}\right)_{\varepsilon=\text{const.}} = 0. \tag{4}$$

We show in Appendix A that this criterion is equivalent to the criterion derived for the steady state growth mechanism of multiple cracks in the weak layer that start from relatively large initial flaws. The underlying assumption is that for a high flaw density, and flaw dimensions of the order of the weak layer thickness t_2, multiple cracking is expected to be growth-controlled and not initiation-controlled. In other words, at all positions in the weak layer where steady state cracks are capable of growing across the specimen width b, they are indeed initiated from existing flaws.

3. Analysis

3.1. Scheme of the analysis

The general sequence of the analysis is as follows: Firstly, using the cracking criterion Eq. (4), the crack density evolution with increasing applied strain is evaluated. This result can in turn be used to generate the stress–strain curve. Finally, using the failure criterion Eq. (1), the applied strain and critical stress at failure are determined, from which the work of fracture is calculated.

Before proceeding, we introduce a normalized crack length $c = t_2/t$. We will restrict the analysis to one particular crack length $c = \frac{1}{2}$. The crack surface energy of the multiply cracked specimen is written as

$$U_{\text{surface}} = (L/a)2\gamma_2 t_2 b = Lb2\gamma_2 cn, \tag{5}$$

where L/a represents the total number of cracks, and $2\gamma_2 t_2 b$ represents the surface energy of a single crack. The strain energy is written in terms of the strain energy of the uncracked specimen multiplied by a dimensionless function of crack density and crack length, $f(n, c)$.

$$U_{\text{strain}} = Lbt\frac{E\varepsilon^2}{2(1-\nu^2)}f(n, c). \tag{6}$$

An analogous factorization is possible for the applied stress σ as a function of applied strain ε. As shown in Appendix B, the dimensionless function of crack density and crack length is identical to $f(n, c)$:

$$\sigma = \frac{E\varepsilon}{1-\nu^2}f(n, c). \tag{7}$$

Finally, the stress intensity factor is written as

$$K_{\text{I}} = \frac{E\varepsilon}{1-\nu^2}t^{1/2}k(n, c), \tag{8}$$

where the factor $(1-\nu^2)$ is introduced for the sake of convenience. In a strict sense, the shape functions $f(n, c)$ and $k(n, c)$ also depend on the Poisson ratio. This dependence is much less pronounced than the influence of crack density and

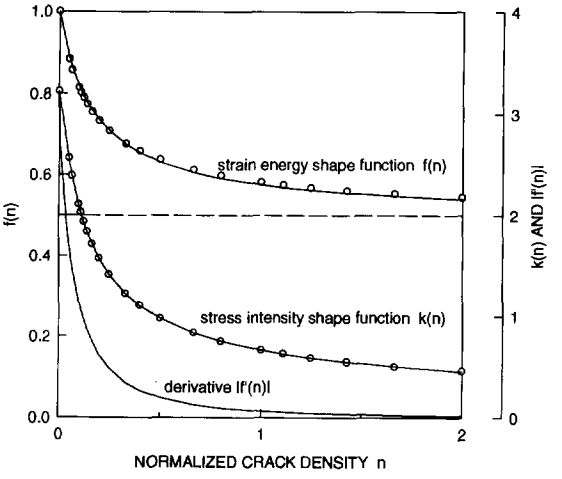

Fig. 5. Shape functions for strain energy $f(n)$ and stress intensity $k(n)$. According to Eqs. (6) and (8), these functions take into account the effect of multiple cracking on strain energy and stress intensity. In addition to $f(n)$, the derivative $|f'(n)|$ is also shown, which governs the crack density evolution in Eq. (11).

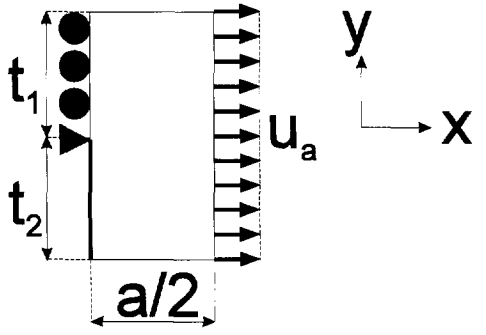

Fig. 6. Unit cell used in the finite element calculation of the shape functions $f(n)$ and $k(n)$. Due to symmetry, only one crack needs to be considered, which is shown by a thicker line. Data points were obtained by changing the unit cell length $a/2$ (a is the crack spacing); the unit cell dimensions $t_1 = t_2 = \frac{1}{2}$ are constant. The right hand side of the unit cell is subject to constant x-displacements u_a, while the left hand side above the crack tip is fixed in the x-direction (solid circles). The crack tip is also fixed in y-direction (solid triangle).

crack length and hence will be neglected (we use $\nu = 0.3$).

The shape functions $f(n, \frac{1}{2}) \equiv f(n)$ and $k(n, \frac{1}{2}) \equiv k(n)$ were obtained using the finite element method by interpolation between f- and k-values for a number of crack densities (Fig. 5). Because of the symmetry of the configuration shown in Fig. 4, the behavior of the entire sample can be characterized by the behavior of the unit cell shown in Fig. 6. The x-displacements of all nodes along the left hand boundary of the unit cell, above the crack tip, were set equal to zero, whereas the right hand boundary was subject to a uniform displacement u_a. The crack tip was fixed in both directions to remove rigid body degrees of freedom. Singular quarter-node elements at the crack tip were used to capture the stress singularity. The stress intensity K_I was estimated by evaluating the x-displacements at the quarter-nodes, and the strain energy per crack was calculated as Fu_a, where F denotes the sum of all nodal forces at the right hand boundary in the x-direction. Substituting these values and $\varepsilon = 2u_a/a$ for the applied strain into Eqs. (6) and (8), the shape functions $f(n)$ and $k(n)$ can be found for all crack densities $n = t/a$. $f(n)$ and $k(n)$ can be approximated by:

$$f(n) = \frac{1}{2}\left(1 + \frac{1}{1 + 2\,|\,f'(0)\,|\,n}\right), \tag{9a}$$

$$k(n) = k(0) \cdot \left(\frac{1 + pn}{1 + qn + rn^2}\right)^{1/2}, \tag{9b}$$

where $f'(0) = -2.8$, $k(0) = 3.2$, $p = 2.8$, $q = 12.3$ and $r = 77.1$. These fitting functions were obtained as Padé-approximations, taking into account the asymptotic behavior for $n \to 0$ and for $n \to \infty$. The value of the strain energy for $n \to 0$ approaches that of an uncracked beam of thickness t, $f(n) = 1$, and for $n \to \infty$ that of a beam with an effective thickness $t/2$, $f(n) = \frac{1}{2}$. The known stress intensity of a singly cracked beam in tension [5] agrees with the $k(0)$-value, and the asymptotics $k(n) \propto n^{-1/2}$ at $n \to \infty$ corresponds to the limit $a \to 0$ in Eq. (2).

For further reference, we mention here also that stresses and strains can be derived from the

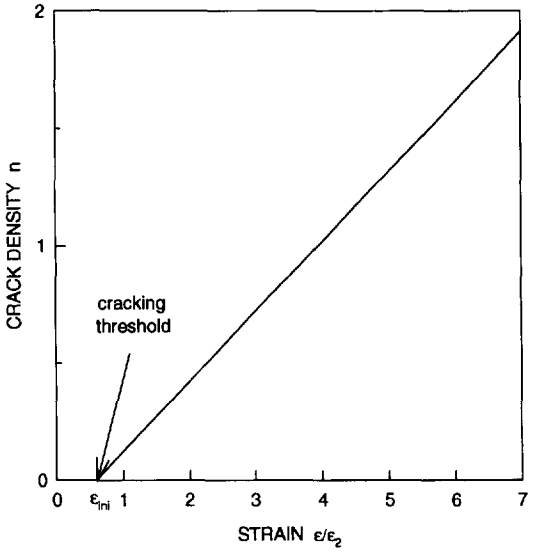

Fig. 7. Crack density evolution as function of applied strain. The crack density n is given as the ratio of beam thickness t to crack spacing a; the strain is normalized on $\varepsilon_2 = (1 - \nu^2)K_{c2}/Et^{1/2}$, where K_{c2}, E and ν are fracture toughness of the weak layer, Young's modulus and Poisson ratio, respectively. At strains $\varepsilon < \varepsilon_{ini}$, insufficient strain energy is available to drive multiple cracks across the specimen width.

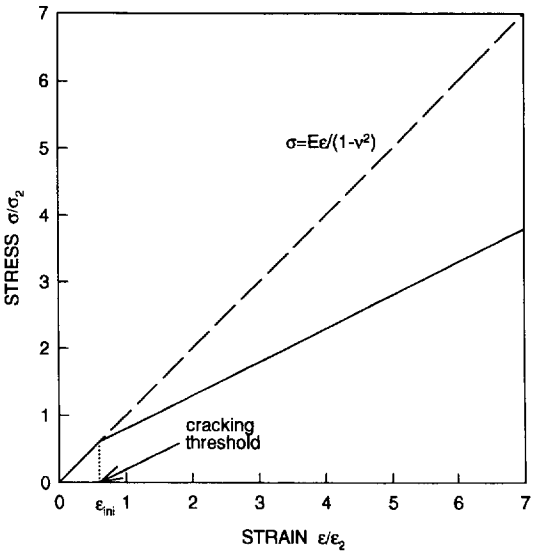

Fig. 8. Applied stress σ as function of applied strain ε. Stress and strain are normalized on $\sigma_2 = K_{c2}/t^{1/2}$ and $\varepsilon_2 = (1-\nu^2)K_{c2}/Et^{1/2}$ where K_{c2}, E, ν and t are fracture toughness of the weak layer, Young's modulus, Poisson ratio and beam thickness, respectively. $\sigma = E\varepsilon/(1-\nu^2)$ indicates the linear stress–strain relation of the uncracked beam.

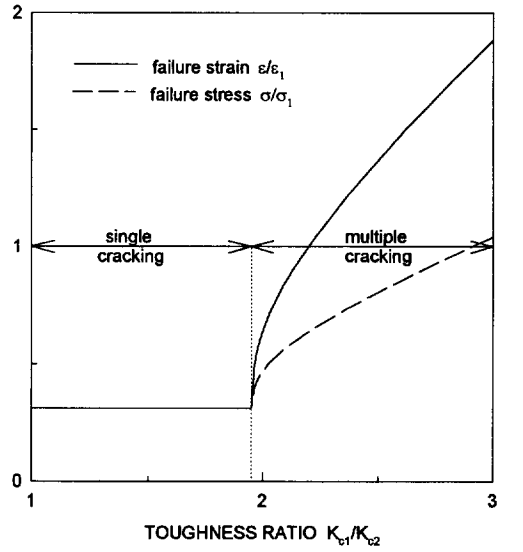

Fig. 9. Failure strain and failure stress as functions of the toughness ratio of the strong and weak layers, K_{c1}/K_{c2}. Stress and strain are normalized on $\sigma_1 = K_{c1}/t^{1/2}$ and $\varepsilon_1 = (1-\nu^2)K_{c1}/Et^{1/2}$, where K_{c1}, E, ν and t are fracture toughness of the tough layer, Young's modulus, Poisson ratio and beam thickness, respectively.

material parameters that characterize the cracking resistance of the strong layer and the weak layer, respectively.

$$\varepsilon_i = \frac{(1-\nu^2)K_{ci}}{Et^{1/2}}, \tag{10a}$$

$$\sigma_i = \frac{K_{ci}}{t^{1/2}}, \tag{10b}$$

where $i = 1, 2$. ε_2 and σ_2 are useful for presenting the crack density evolution in the weak layer and the stress–strain curve, which is influenced by the crack-induced stiffness loss of the weak layer. Similarly, the ultimate failure strain and stress depend upon the fracture toughness of the strong layer, K_{c1}, and therefore are conveniently normalized by ε_1 and σ_1. The work of fracture, W_{fracture}, scales with the sample length L and the width b. Hence, the combination $Lb\gamma_1$, where γ_1 is the surface energy per unit crack area in the strong layer, is an appropriate normalizing quantity for the work of fracture, since it allows us to relate the work of fracture of a multiply cracked specimen, which is composed of a strong layer

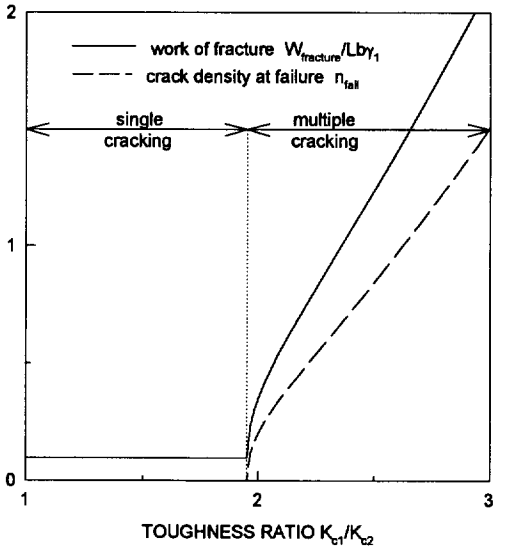

Fig. 10. Crack density at failure and work of fracture as functions of the toughness ratio of the strong and weak layers, K_{c1}/K_{c2}. The crack density n is given as the ratio of beam thickness t to crack spacing a; the work of fracture is normalized on the crack surface energy of the tough layer, γ_1, times beam length L and beam width b.

and a weak layer, to the work of fracture of a homogeneous singly cracked specimen which is characterized by the crack surface energy γ_1.

3.2. Crack density evolution and stress–strain curve

Eqs. (4), (5) and (6) with $c = 0.5$ provide the following equation:

$$f'(n) = -\frac{1}{(\varepsilon/\varepsilon_2)^2}, \tag{11}$$

where the characteristic strain ε_2 is defined by Eq. (10). Substituting Eq. (9) into (11) we obtain the crack-density–strain relation (Fig. 7)

$$n(\varepsilon/\varepsilon_2) = \begin{cases} 0 & \text{for } \varepsilon \le \varepsilon_{ini}, \\ \dfrac{\varepsilon_{ini}}{2\varepsilon_2}\dfrac{\varepsilon - \varepsilon_{ini}}{\varepsilon_2} & \text{for } \varepsilon \ge \varepsilon_{ini}, \end{cases} \tag{12a}$$

$$\varepsilon_{ini} = \frac{\varepsilon_2}{|f'(0)|^{1/2}} \approx 0.6 \cdot \frac{(1-\nu^2)K_{c2}}{Et^{1/2}}. \tag{12b}$$

ε_{ini} characterizes the minimum strain which is necessary to initiate multiple cracking. The existance of this threshold strain becomes clear, as the right hand side of Eq. (11) diverges for $\varepsilon \to 0$, but the left hand side remains finite ($|f'(n)| \le |f'(0)| = 2.8$); thus the cracking condition Eq. (11) has no solution for small strains. This means physically that the available strain energy release at low strains is not sufficient to form a regular array of multiple cracks which are separated by finite crack spacings.

Finally, the stress–strain curve, which is plotted in Fig. 8, is obtained by substituting the crack density function $n(\varepsilon)$ into Eq. (7):

$$\sigma = \frac{E}{1-\nu^2} \times \begin{cases} \varepsilon & \text{for } \varepsilon \le \varepsilon_{ini}, \\ (\varepsilon + \varepsilon_{ini})/2 & \text{for } \varepsilon \ge \varepsilon_{ini}. \end{cases} \tag{13}$$

3.3. Failure stress, failure strain and work of fracture

The failure condition (1), combined with Eq. (8) for the stress intensity, leads to the following equation for the failure strain ε_{fail}:

$$1 = \frac{\varepsilon_{fail}}{\varepsilon_1} k(n(\varepsilon_{fail}/\varepsilon_2)), \tag{14}$$

where $n(\varepsilon_{fail}/\varepsilon_2)$ represents the function given by Eq. (12) with $\varepsilon = \varepsilon_{fail}$. According to Eq. (10), we can replace $\varepsilon_{fail}/\varepsilon_2$ by the product $(\varepsilon_{fail}/\varepsilon_1)(K_{c1}/K_{c2})$ and solve Eq. (14) for the normalized failure strain as a function of the toughness ratio $\varepsilon_{fail}/\varepsilon_1 = \varphi(K_{c1}/K_{c2})$ (Fig. 9). Obviously, the failure strain has to exceed the threshold strain for multiple cracking if multiple cracking is to be initiated prior to failure. Inserting $\varepsilon_{fail} > \varepsilon_{ini}$ into Eq. (14) and using ε_{ini} from Eq. (12), this condition can be formulated in terms of the toughness ratio K_{c1}/K_{c2}:

$$\frac{K_{c1}}{K_{c2}} > \frac{k(0)}{|f'(0)|^{1/2}} \approx 1.9. \tag{15}$$

The normalized failure strain, $\varepsilon_{fail}/\varepsilon_1 = \varphi(K_{c1}/K_{c2})$, combined with Eq. (11), leads to an equation which determines the crack density at failure, $n_{fail}/n_{fail} = (K_{c1}/K_{c2})$:

$$f'(n_{fail}) = -\frac{1}{(K_{c1}/K_{c2})^2 \varphi^2(K_{c1}/K_{c2})}. \tag{16}$$

The solution of Eq. (16) is plotted in Fig. 10. Now, substituting crack density at failure, $n_{fail}(K_{c1}/K_{c2})$, and failure strain, $\varepsilon_{fail}/\varepsilon_1 = \varphi(K_{c1}/K_{c2})$, into Eq. (7), the failure stress can be deduced as function of the toughness ratio K_{c1}/K_{c2} (Fig. 9) [1].

Generally, the work of fracture, $W_{fracture}$, which has to be calculated by integration of the stress–strain curve (Fig. 8) in the range $0 \le \varepsilon \le \varepsilon_{fail}$, exceeds the total energy at failure due to additional energy dissipation (for example by unstable cracking). However, taking into account the steady state character of multiple cracking, the work of

[1] The dependence of failure strain and stress on the toughness ratio are most conveniently expressed in a parametric form, using the following equations: $K_{c1}/K_{c2} = (\varepsilon(n_{fail})/\varepsilon_2)\, k(n_{fail})$, $\varepsilon_{fail}/\varepsilon_1 = 1/k(n_{fail})$ and $\sigma_{fail}/\sigma_1 = f(n_{fail})/k(n_{fail})$. These equations follow directly from the definition of the shape functions and of the constants $\varepsilon_1, \sigma_1, \varepsilon_2, \sigma_2$.

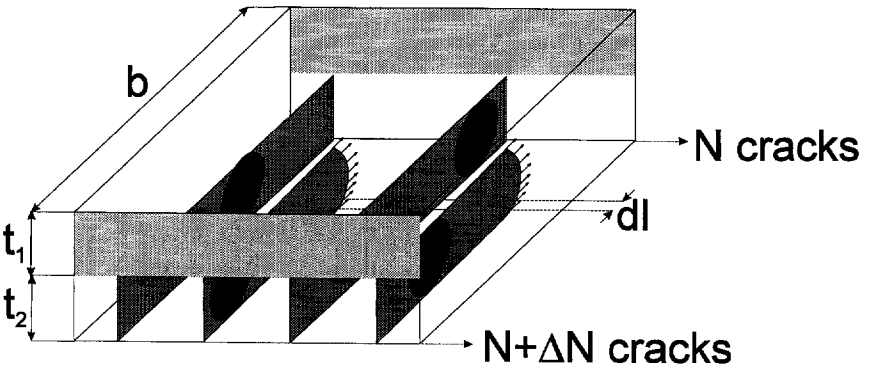

Fig. 11. Steady state growth of ΔN cracks between N pre-existing cracks. Cracks are shown by the grey pattern, and the crack-initiating penny-shaped flaws are shown in black. The crack front propagates by an increment dl. b, t_1 and t_2 indicate specimen width, the thickness of the tough layer and of the multiply cracked weak layer, respectively.

fracture can be shown to be equal to the total energy at failure [2].

$$U_{\text{total}}(\varepsilon_{\text{fail}}) = \int_0^{\varepsilon_{\text{fail}}} \left(\frac{\partial U_{\text{total}}}{\partial \varepsilon}\right)_n \mathrm{d}\varepsilon = Lbt\int_0^{\varepsilon_{\text{fail}}} \sigma \,\mathrm{d}\varepsilon = W_{\text{fracture}}. \tag{17}$$

Thus the work of fracture is given by the sum of crack surface energy plus strain energy at failure. Normalized by $Lb\gamma_1$, it can be expressed in terms of the toughness ratio K_{c1}/K_{c2} (Fig. 10):

$$\frac{W_{\text{fracture}}}{Lb\gamma_1} = \varphi^2(K_{c1}/K_{c2}) f(n_{\text{fail}}(K_{c1}/K_{c2})) + \frac{n_{\text{fail}}(K_{c1}/K_{c2})}{(K_{c1}/K_{c2})^2}. \tag{18}$$

4. Discussion

The results of the previous analysis can be summarized by the following statements.

1. Mutual stress relief of externally loaded multiple cracks leads to a higher failure stress and strain compared to singly cracked specimens. The failure strain increases further due to stiffness loss of multiply cracked specimens. The combined effect of failure stress and strain results in a high work of fracture.

2. Multiple cracking is favored by the presence of a protective weak layer with low fracture toughness. The proposed mechanism assumes the presence of a sufficient number of relatively large initial defects in this layer which, if externally loaded, can grow as steady state cracks to their final size.

3. A minimum strain and a minimum ratio of the strong layer fracture toughness to the weak layer fracture toughness, K_{c1}/K_{c2}, are required to cause multiple cracking.

4. For an increasing ratio K_{c1}/K_{c2}, at constant strong layer toughness K_{c1}, the work of fracture grows apparently without limit. In other words, for $K_{c2} \to 0$, the numerous multiple cracks which form in the weak layer have no effect on the strong layer in the sense of failure-causing defects.

Of course, the question arises, why is the weak layer necessary at all? One possible reason for the conch shell, which inspired us in particular to postulate this mechanism, could be that growth imperfections or environmentally induced flaws always exist in the shell. If subject to external loading by predators, such flaws are quite danger-

[2] The derivation of Eq. (17) uses 2 conditions, the steady state criterion, Eq. (4), and the relation between total energy and applied stress:

$$\left(\frac{\partial U_{\text{total}}}{\partial \varepsilon}\right)_n = \left(\frac{\partial U_{\text{strain}}}{\partial \varepsilon}\right)_n = Lbt\sigma.$$

ous in a homogeneous material as they lead to catastrophic failure at critical loads, which are limited by the characteristic strength of the *material* [3]. This 'material-inherent strength' is enhanced significantly in the shell by using the hierarchical composite *structure* optimized by nature over millions of years.

In the light of these considerations a flaw-rich microstructure, corresponding to our postulated growth-controlled cracking regime, should be advantageous compared to an almost flaw-free structure which corresponds to an initiation-controlled mechanism and thus is more susceptible to catastrophic failure. To some extent this situation was investigated already in Ref. [4]; that model will be addressed in a future paper. Additionally, toughness-enhancing mechanisms like crack bridging and microcracking are undoubtedly effective in fracture of the conch shell [4] and must be considered as well.

Finally, we want to emphasize the similarity of our model for multiple cracking with the investigation of multiple cracking in thin films on a substrate by Thouless et al. [7]. Differences are due to the fact that the 'weak' layer and 'tough' layer in the shell are of comparable thicknesses and consist essentially of the same material; the different toughnesses are caused by the orientations of the 1st-order lamellae in the 'weak' layer which are perpendicular to the corresponding orientation in the 'tough' layer. Furthermore, the composite structure of the conch shell is composed of at least three layers with differing orientations. Possibly, this makes the toughening effect by multiple cracking more independent on the orientation of the external load with respect to the orientation of the layers.

Acknowledgements

H. Kessler appreciates useful discussions with H. Balke, Technical University Dresden, and H.-A. Bahr, Max Planck Research Group 'Mechanics of Heterogeneous Solids' in Dresden. His participation in this research was enabled by a Feodor–Lynen Fellowship of the Alexander von Humboldt Foundation in Germany. The present work was supported by the Department of Energy through a grant to Batelle's Pacific Northwest Laboratory.

[3] The term 'material' is used here in the sense of a material itself, plus its inherent defect structure.

Appendix A. Steady state character of the cracking condition Eq. (4)

Consider ΔN stably growing cracks between N pre-existing cracks that span the total specimen width b and the thickness of the weak layer t_2 (Fig. 11). Using the concept of steady state cracking [6], the change of the total energy corresponding to a virtual increment $\mathrm{d}l$ of the ΔN propagating cracks can be expressed as

$$\mathrm{d}U_{\text{total}} = \left(\Delta N 2\gamma_2 t_2 + \frac{U_{\text{strain}}(N+\Delta N) - U_{\text{strain}}(N)}{b} \right) \mathrm{d}l, \tag{A.1}$$

where γ_2 denotes the specific surface energy per crack area in the weak layer. The 1st term in Eq. (A.1) gives the increment of crack surface energy and needs no further explanation. The 2nd term in Eq. (A.1) gives the (negative) strain energy increment; this will become clear in the following. Close to the front of the ΔN propagating cracks, the state of stress is 3-dimensional. This complex stress state moves together with the crack front; in other words, it remains unchanged in the moving coordinate system connected to one of the crack tips. Behind the crack front, at distances exceeding the layer thickness t_2, the stress state remains plane strain, as in a sample with $N + \Delta N$ cracks spanning the total width. Similarly, the stress state is still plane strain at distances exceeding t_2 ahead of the crack tip, as in a sample with N plane strain cracks. The change of strain energy due to the increment $\mathrm{d}l$ of the crack front can be obtained if we 'slice' a part $\mathrm{d}l$ of the

specimen at the edge with N cracks, introduce ΔN additional cuts and then 'glue' it to the opposite-edge with $N+\Delta N$ cracks. Obviously, the strain energy increment for this operation is equal to the length dl times the difference of the strain energy per width, $U_{\text{strain}}(N+\Delta N)/b$ of a sample with $N+\Delta N$ cracks minus the strain energy per width, $U_{\text{strain}}(N)/b$, of a sample with N cracks.

Stable cracking means that the released strain energy is consumed by the increasing crack surface energy ($dU_{\text{total}}=0$). Using this condition and expanding the strain energy difference in Eq. (A.1) to 1st order accuracy with respect to ΔN, we arrive at the steady state criterion

$$2\gamma_2 t_2 b + \left(\frac{\partial U_{\text{strain}}}{\partial N}\right)_{\varepsilon=\text{const.}} = 0. \tag{A.2}$$

This is equivalent to the energy minimum criterion of Eq. (4). It is only approximate as, in a rigorous sense, a power series expansion of the strain energy difference in Eq. (A.1) is justified only for a small number of growing cracks $\Delta N \ll N$, in contrast to the configuration depicted in Fig. 11, where $\Delta N = N$. Eq. (4) would be the exact steady state criterion if multiple cracking would be a continuous rather than a discrete process.

Appendix B. Shape functions of strain energy and applied stress

Hill's theorem allows us to split the strain energy in a certain volume V into a product of average stresses and average strains, $U_{\text{strain}}(V) = V\bar{\sigma}_{ij}(V)\bar{\varepsilon}_{ij}(V)/2$ [8]. When applied to a unit cell of our tensile specimen with one crack and a volume $V=(a/2)tb$ (Fig. 6), this equation simplifies by virtue of symmetry to

$$U_{\text{strain}} = \frac{atb\sigma\varepsilon}{4}. \tag{A.3}$$

In Eq. (A.3) the equivalence of average and applied stresses or strains is used, that is $\sigma=\bar{\sigma}_{xx}$ and $\varepsilon=\bar{\varepsilon}_{xx}$. A comparison of Eq. (A.3) with Eq. (6) or (7), taking into account the unit cell length $L=a/2$, shows that applied stress and strain energy must have identical shape functions.

References

[1] A.G. Evans and K.T. Faber, J. Am. Ceram. Soc. 67 (4) (1984) 255.
[2] J.D. Currey and A.J. Kohn, J. Mater. Sci. 11 (1976) 1615.
[3] V.J. Laraia, M. Aindow and A.H. Heuer, Mater. Res. Soc. Symp. Proc. 174 (1990).
[4] L.T. Kuhn, H. Kessler, S.M. Spearing and A.H. Heuer, J. Mater. Sci., to be published.
[5] X.-R. Wu and A.J. Carlsson, Weight Functions and Stress Intensity Factor Solutions (Pergamon Press, Oxford, 1991).
[6] J.W. Hutchinson and Z. Suo, Advances in Applied Mechanics 29 (1990) 63.
[7] M.D. Thouless, E. Olsson and A. Gupta, Acta Metall. Mater. 40 [6] (1992) 1287.
[8] R. Hill, J. Mech. Phys. Solids 11 (1963) 357.